ChemComm

COMMUNICATION

View Article Online
View Journal | View Issue



Cite this: *Chem. Commun.*, 2025, **61**, 11846

Received 29th May 2025,
Accepted 2nd July 2025

DOI: 10.1039/d5cc03044g

rsc.li/chemcomm



# Isostructural chiral metal–organic frameworks for enantioselective luminescence sensing of 1-phenyl-1,2-ethanediol†

Chenghua Deng, Zitong Wang, Jinhong Li and Wenbin Lin *

**We report the synthesis of isostructural chiral metal–organic frameworks (CMOFs), Zn–L–(Et)$_2$, Zn–L–Me and Zn–L, based on $Zn_2$ paddle-wheel secondary building units and three 1,1′-bi-2-naphthol (BINOL)-derived tetrabenzoate ligands [L–(Et)$_2$, L–Me, and L], featuring different alkyl substituents at the 2,2′-hydroxyl positions. These CMOFs were evaluated as luminescent sensors for the enantiomers of 1-phenyl-1,2-ethanediol (PE). All three CMOF sensors exhibited selective quenching of *S*-PE over *R*-PE, with significantly higher quenching efficiencies than their corresponding free ligands. The presence of hydroxyl groups induced nonlinear quenching behaviour toward *S*-PE, further enhancing quenching efficiency. Notably, Zn–L–Me and Zn–L showed exponential quenching responses as a function of enantiomeric excess (ee) at a PE concentration of 1.6 mM.**

Due to the mirror-image geometries, chiral enantiomers often exhibit markedly different properties in applications such as pharmaceuticals, pesticides, and optical devices.[1,2] The sensing, separation, and catalytic synthesis of chiral compounds are critical yet challenging areas in chemistry.[1–3] Metal–organic frameworks (MOFs) are rapidly emerging as versatile porous materials with broad applications, including gas storage and separation, drug delivery, bioimaging, catalysis, and chemical sensing, owing to their desirable features such as high crystallinity, large surface area, tunable open metal sites, and customizable functional groups.[4–14] Among these, the luminescent properties of MOFs are particularly valuable, as they can reveal specific host–guest interactions with target molecules within their pores, leading to measurable spectroscopic changes such as fluorescence quenching or enhancement.[15,16] These photophysical responses position luminescent MOFs as effective platforms for the rapid and selective detection of chiral compounds, offering a promising approach for enantiomeric sensing.[17,18]

Chiral metal–organic frameworks (CMOFs) constructed from chiral ligands, particularly derivatives of 1,1′-bi-2-naphthol (BINOL), have shown great promise in a variety of applications, including asymmetric catalysis, nonlinear optics, enantiomer separation, absolute structure determination, and chiral sensing.[16,19–24] The incorporation of well-defined chiral binding sites within CMOFs facilitates selective interactions with target enantiomers, markedly enhancing fluorescence detection efficiency compared to conventional homogeneous sensing systems.[23–27] Our group previously developed a cadmium-based CMOF using the *R*-2,2′-BINOL-4,4′,6,6′-tetra benzoic acid ($H_4$**L**) ligand, formulated as $\{[Cd_2(\mathbf{L})(H_2O)_2]\cdot 6.5DMF\cdot 3EtOH\}_n$, in which cadmium ions are assembled into rod-shaped secondary building units (SBUs). We explored its fluorescence quenching behaviour toward the enantiomers of amino alcohols, demonstrating its potential as a selective chiral sensor.[24]

The enantiomers of 1-phenyl-1,2-ethanediol (PE) are important building blocks in the synthesis of several drugs such as Mirogabalin, amido thiadiazole and nicotinamide derivatives.[28–30] CMOFs such as $[In_3O(obb)_3(HCO_2)(H_2O)]_n$ and $\{(Me_2NH_2)_2[Mn_4O(d\text{-cam})_4]\cdot(H_2O)_5\}_n$ have been used as stationary phases for the chromatographic separation of racemic PE.[31,32] We previously reported a zinc-based CMOF, $\{[Zn_2(\mathbf{L})(DMF)(H_2O)](DMF)_{5.7}\}_n$ (Zn–**L**), derived from the $H_4$**L** ligand, as well as its Ti(OiPr)$_4$-modified analogue, for enantioselective catalysis of the addition of diethylzinc to aromatic aldehydes to generate chiral secondary alcohols.[33] In Zn–**L**, $Zn_2$ paddle-wheel SBUs and 4-connected (4-c) **L** ligands form a two-fold interpenetrated 4-c **unc** network (Fig. S3, ESI†).[33] In the present study, we investigate Zn–**L** and its isostructural CMOFs for luminescent sensing of PE enantiomers (Fig. 1).

$H_4$**L** and *R*-2,2′-diethoxy-BINOL-4,4′,6,6′-tetrabenzoic acid [$H_4$**L**–(Et)$_2$] were prepared *via* Suzuki coupling followed by hydrolysis (Fig. S1 and S4–S8, ESI†). *R*-2-methoxy-BINOL-4,4′,6,6′-tetrabenzoic acid ($H_4$**L**–Me) was obtained through iterative protection and deprotection of the carboxylic acid and hydroxy groups on $H_4$**L** (Fig. S2 and S9–S12, ESI†). The corresponding CMOFs, Zn–**L**, $\{[Zn_2(\mathbf{L}\text{–}(Et)_2)(DMF)(H_2O)](DMF)_{5.4}\}_n$ (Zn–**L**–(Et)$_2$)

*Department of Chemistry, The University of Chicago, Chicago, Illinois 60637, USA. E-mail: wenbinlin@uchicago.edu*

† Electronic supplementary information (ESI) available. See DOI: https://doi.org/10.1039/d5cc03044g

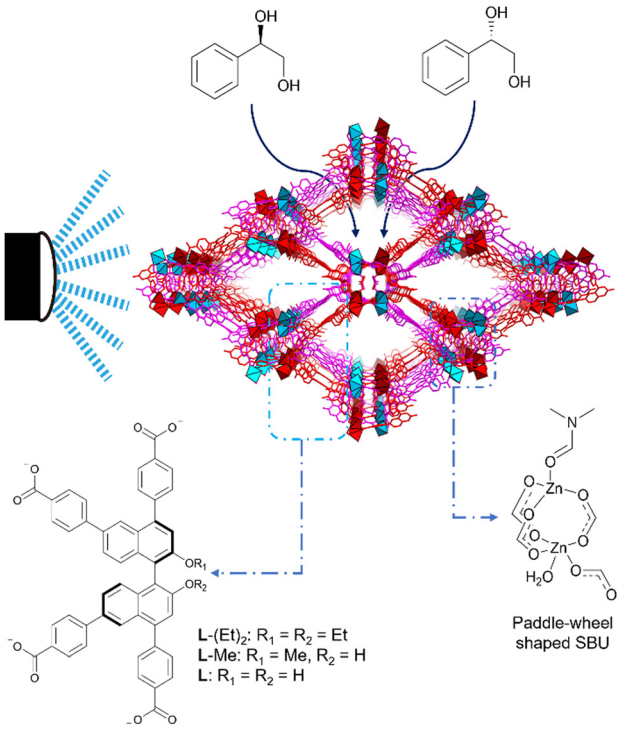


Fig. 1 Schematic illustration of isostructural CMOFs built from $Zn_2$ paddle-wheel SBUs and BINOL-based tetrabenzoate ligands and their application in luminescence sensing of PE enantiomers.

and $\{[Zn_2(\mathbf{L}\text{–Me})(DMF)(H_2O)](DMF)_5\}_n$ (Zn–**L**–Me) were prepared *via* solvothermal reactions of $ZnI_2$ with the respective ligands (Fig. 1 and Fig. S3, ESI†). The chemical compositions of the CMOFs were determined by $^1$H NMR spectra of digested samples (Fig. S13–S15, ESI†). Crystallinity and phase purity were confirmed by powder X-ray diffraction (PXRD) analysis (Fig. S16, S18 and S19, ESI†). Structural models of Zn–**L**–$(Et)_2$ and Zn–**L**–Me were derived from Zn–**L**, and then refined through energy minimization, geometry optimization, and Pawley refinement using the Forcite and Reflex modules in the Materials Studio software (Fig. S16, S19 and Tables S1, S2, ESI†). For luminescence quenching studies, all ligands and CMOFs were dispersed in acetonitrile at a ligand concentration of 31.4 μM.

The excitation spectra of $H_4$**L**–$(Et)_2$, $H_4$**L**–Me and $H_4$**L** exhibited absorption maxima at 366, 359 and 350 nm, respectively (Fig. 2). At their corresponding excitation wavelengths, these ligands showed emission maxima at 443 nm ($H_4$**L**–$(Et)_2$) and 440 nm ($H_4$**L**–Me and $H_4$**L**). In comparison, the excitation maxima of Zn–**L**–$(Et)_2$, Zn–**L**–Me and Zn–**L** were slightly red-shifted to 372, 372, and 365 nm, respectively (Fig. 2), with corresponding emission maxima red-shifted to 453, 455 and 454 nm. These excitation wavelengths were used in all subsequent luminescence sensing experiments. The CMOF suspensions exhibited stable luminescence signals with less than 8% intensity fluctuation over 30 minutes (Fig. S23, ESI†).[33]

With increasing concentrations of *R*-PE, the BINOL-derived ligands showed nearly linear Stern–Völmer (S–V) quenching behaviour (Fig. S24–S26, ESI†).[34] The S–V constants ($K_{sv}$) for

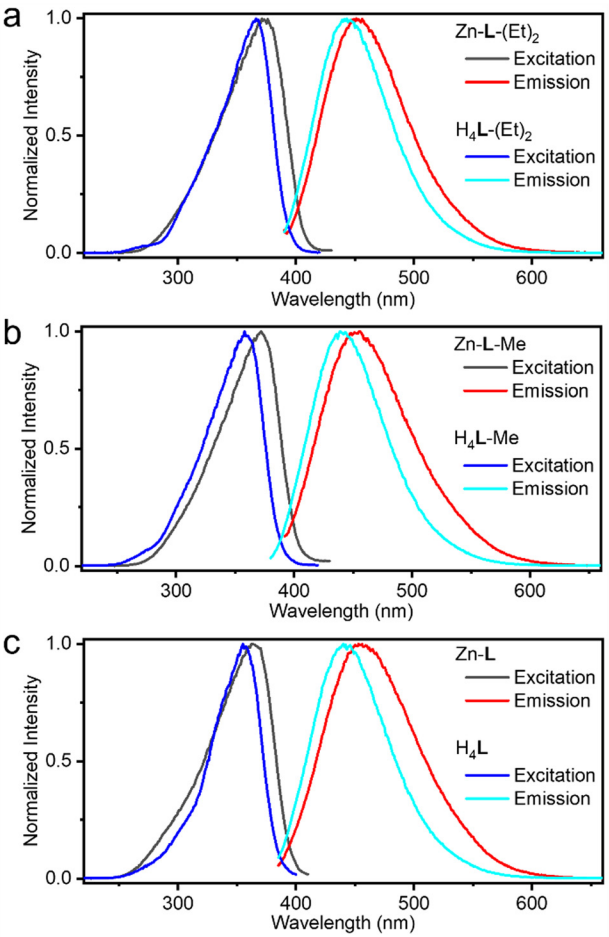


Fig. 2 Excitation and emission spectra of CMOFs and ligands, (a) Zn–**L**–$(Et)_2$ and $H_4$**L**–$(Et)_2$, (b) Zn–**L**–Me and $H_4$**L**–Me, (c) Zn–**L** and $H_4$**L**.

$H_4$**L**–$(Et)_2$, $H_4$**L**–Me and $H_4$**L** were determined to be 3.80 ± 1.6, 26.9 ± 1.4, and 57.0 ± 2.0 $M^{-1}$, respectively (Fig. 3a, c and e and Table S3, ESI†), corresponding to quenching efficiencies of 1%, 4.6% and 7.5% at 1.6 mM *R*-PE. Both $K_{sv}$ constants and quenching efficiencies increased with the number of hydroxy groups on the sensor ligands. For *S*-PE, $H_4$**L**–$(Et)_2$ showed a much stronger linear quenching response, with a $K_{sv}$ value of 244 ± 4.3 $M^{-1}$ and a quenching ratio (QR, $K_{sv}(S)/K_{sv}(R)$) of 64, indicating that even the *R*-BINOL ligand lacking hydroxy substituents exhibited a strong enantioselective interaction with *S*-PE over *R*-PE.

$H_4$**L**–Me and $H_4$**L** exhibited nonlinear quenching behaviour upon increasing concentrations of *S*-PE (Fig. S25 and S26, ESI†). Their S–V plots showed pronounced upward curvature (Fig. 3c and e) and could not be fitted by the standard static-dynamic combination quenching model: $I_0/I = (1 + K_{sv}[M])\exp(V[M])$.[34,35] To account for this deviation, we propose a dynamic factor-enhanced static-dynamic combination model: $I_0/I = (1 + K_{sv}[M])(c\exp(V[M]) + 1-c)$,[34,36] where a weighting factor $c$ was introduced to represent the fraction of fluorophores undergoing static-like quenching. In this model, $K_{sv}$ ($M^{-1}$) is the dynamic quenching constant, $V$ ($M^{-1}$) is the

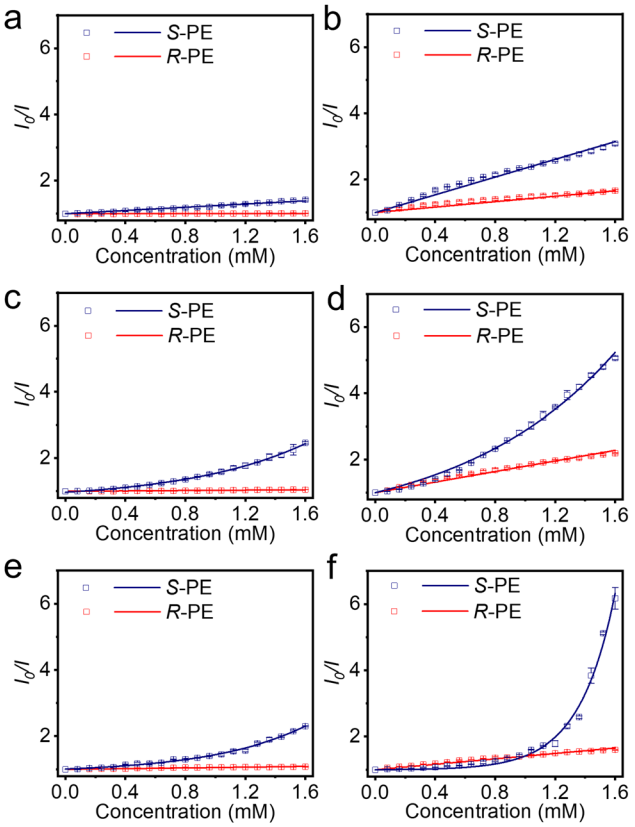


Fig. 3 Stern–Völmer plots (points for data and lines for fitting) for $H_4$**L**–$(Et)_2$ (a), Zn–**L**–$(Et)_2$ (b), $H_4$**L**–Me (c), Zn–**L**–Me (d), $H_4$**L** (e) and Zn–**L** (f) with increasing concentrations of *R*-PE and *S*-PE.

volume constant corresponding to the active volume surrounding the excited fluorophore, and $c$ is the fractional contribution of static quenching. Using this model, the extracted $K_{sv}$ values for $H_4$**L**–Me and $H_4$**L** were $5.52 \times 10^{-12}$ and $182 \pm 74$ $M^{-1}$, respectively. The corresponding $V$ values were 1375 and 1938 $M^{-1}$, and the $c$ values were $0.181 \pm 0.013$ and $(3.73 \pm 2.6) \times 10^{-2}$, respectively. At 1.6 mM *S*-PE, the quenching efficiencies for $H_4$**L**–Me and $H_4$**L** were 59.4% and 56.5%, substantially higher than that of $H_4$**L**–$(Et)_2$ (29.8%), suggesting the presence of hydroxy groups enhances interaction with *S*-PE, likely *via* hydrogen bonding.

With increasing *R*-PE concentration, all CMOFs exhibited linear S–V quenching behaviour (Fig. 3b, d, f and Fig. S27–S29, ESI†).[29] The $K_{sv}$ constants for Zn–**L**–$(Et)_2$, Zn–**L**–Me, and Zn–**L** were determined to be $448 \pm 11$, $800 \pm 12$, and $412 \pm 6.6$ $M^{-1}$, respectively (Table S3, ESI†), corresponding to quenching efficiencies of 39.9%, 54.3% and 37.8% at 1.6 mM *R*-PE. For *S*-PE, Zn–**L**–$(Et)_2$ also displayed a linear quenching response with a $K_{sv}$ value of $1342 \pm 18$ $M^{-1}$ (Fig. 3b and Fig. S27, ESI†), yielding a QR ($K_{sv}(S)/K_{sv}(R)$) of 3. In contrast, Zn–**L**–Me and Zn–**L** exhibited nonlinear quenching behaviour in response to *S*-PE (Fig. S28 and S29, ESI†), with quenching efficiencies of 80.2% and 83.8%, respectively, compared to Zn–**L**–$(Et)_2$ (67.5%). These results suggest that hydroxy-functionalized CMOFs enhance interactions with *S*-PE, likely through hydrogen bonding, thereby increasing quenching efficiency. The S–V plot for Zn–**L**–Me was well fitted by the static–dynamic combination quenching model, yielding a $K_{sv}$ constant of $340 \pm 141$ $M^{-1}$ and V constant of $763 \pm 96$ $M^{-1}$ (Fig. 3d and Table S3, ESI†). For Zn–**L**, the S–V plot was best fitted using the dynamic factor–enhanced static–dynamic combination model, providing $K_{sv}$, $V$ and $c$ values of $2.32 \times 10^{-12}$ $M^{-1}$, $4215 \pm 162$ $M^{-1}$, and $(6.27 \pm 1.6) \times 10^{-3}$, respectively (Fig. 3f and Table S5, ESI†). Compared to Zn–**L**–Me, Zn–**L** offers additional hydroxy groups and greater void space, which promote stronger dynamic interactions with *S*-PE and yield superior quenching performance. PXRD analysis confirmed that the crystallinity of the CMOFs was retained after stirring and luminescent sensing experiments (Fig. S17, S18 and S20, ESI†). Compared to their corresponding ligands, the CMOFs generally exhibited enhanced quenching efficiencies, likely due to the adsorption of the analytes in the channels, effectively increasing local analyte concentrations and their supramolecular interactions with the frameworks.

To further investigate the enantioselective quenching efficiencies of the CMOFs, luminescence experiments were performed with PE samples of varying enantiomeric excess (ee) values ($S > R$). Zn–**L**–$(Et)_2$ showed linear S–V behaviour across ee values of −80%, −40%, 0%, 40% and 80%, with corresponding $K_{sv}$ values of $536 \pm 8.5$, $784 \pm 13$, $961 \pm 8.0$, $1064 \pm 12$, and $1211 \pm 6.6$ $M^{-1}$, respectively (Fig. S30, S31 and Table S3, ESI†). At 1.6 mM PE, a plot of $I_0/I$ *versus* % ee revealed a linear relationship with a slope of $6.77 \times 10^{-3}$ and an intercept of 2.441 (Fig. 4a). For Zn–**L**–Me, PE samples with −80% ee produced a linear quenching response with $K_{sv}$ value of $698 \pm 9.1$ $M^{-1}$, while higher ee values followed a static-dynamic combination quenching model (Fig. S32, S33 and Table S4, ESI†). At 1.6 mM PE, the corresponding $I_0/I$ values fit an exponential relationship: $I_0/I = 0.248 \exp(2.43 \times 10^{-2}\%\ ee) + 2.136$ (Fig. 4b). Zn–**L** displayed linear quenching at −80% and

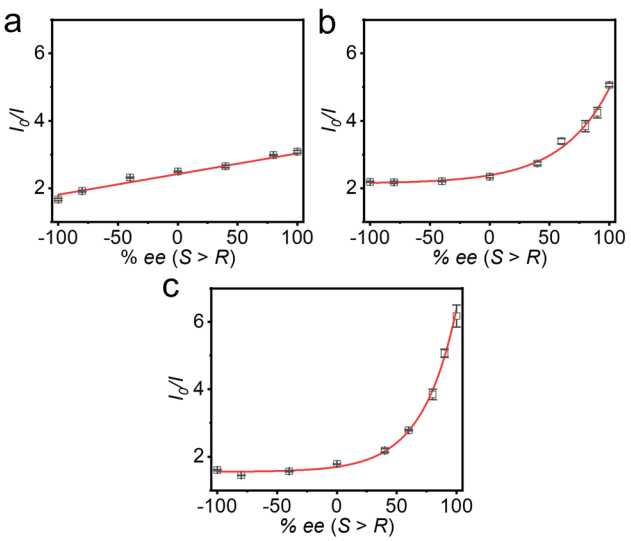


Fig. 4 $I_0/I$ *versus* ee plots of PE for Zn–**L**–$(Et)_2$ (a), Zn–**L**–Me (b), and Zn–**L** (c), at a fixed PE concentration of 1.60 mM.

−40% ee with $K_{sv}$ constants of 280 ± 3.2 and 359 ± 3.4 $M^{-1}$, respectively. For higher ee values, the quenching response followed the dynamic factor–enhanced static–dynamic combination model (Fig. S34, S35 and Table S5, ESI†). At 1.6 mM PE, the $I_0/I$ *versus* % ee relationship fit an exponential function: $I_0/I = 0.174\exp(3.29 \times 10^{-2}\%\ \text{ee}) + 1.536$ (Fig. 4c). Although Zn–**L**–Me and Zn–**L** showed limited quenching responses at low ee values (<0%), their exponential increases at higher ee values make them particularly well-suited for detecting *S*-enriched PE samples. Under UV illumination, changes in quenching efficiency were visually more pronounced for Zn–**L** compared to other CMOFs and free ligands (Fig. S21 and S22, ESI†). We also tested Zn–**L** as a luminescent sensor for the enantiomers of phenylalaniol, phenylglycinol, alaniol, *tert*-leucinol and valinol. However, these analytes did not exhibit significant enantioselectivity in luminescence quenching.

In summary, a series of isostructural Zn-based CMOFs were developed by selectively modifying the two hydroxy groups of Zn–**L** with either two ethoxy or one methoxy substituent. Their luminescent sensing performance toward the enantiomers of PE was systematically investigated. All CMOFs exhibited preferential quenching by *S*-PE over *R*-PE. Upon increasing *S*-PE concentration, Zn–**L**–$(Et)_2$, Zn–**L**–Me, and Zn–**L** followed linear, static–dynamic combination, and dynamic factor-enhanced static–dynamic combination quenching models, respectively. For Zn–**L**–Me and Zn–**L**, the quenching intensities showed exponential dependence on % ee at 1.6 mM PE. The *R*-BINOL-based geometry favored selective interactions with *S*-PE, and the presence of hydroxy groups further enhanced enantioselective quenching, likely through hydrogen bonding. This study highlights the potential of hydroxy-functionalized CMOFs as effective platforms for enhancing host–guest interactions in the enantioselective sensing of pharmaceutically relevant chiral compounds.

Chenghua Deng: conceptualization, methodology, investigation, writing – original draft. Zitong Wang and Jinhong Li: investigation. Wenbin Lin.: supervision, resources, funding acquisition, writing – review & editing.

This work was supported by the University of Chicago.

## Conflicts of interest

The authors declare no competing interests.

## Data availability

The data supporting this article have been included in the ESI.†

## Notes and references

1 C. Wolf, *Dynamic Stereochemistry of chiral compounds: principles and applications*, Royal Society of Chemistry, Cambridge, 2007.
2 A. Satinder, *Chiral separation methods for pharmaceutical and biotechnological products*, John Wiley & Sons, Inc., New Jersey, 2011.
3 Q.-L. Zhou, *Privileged Chiral Ligands and Catalysts*, Wiley-VCH Verlag & Co. KGaA, Germany, 2011.
4 H. Li, L. Li, R.-B. Lin, W. Zhou, Z. Zhang, S. Xiang and B. Chen, *EnergyChem*, 2019, **1**, 100006.
5 J. L. C. Rowsell and O. M. Yaghi, *Angew. Chem., Int. Ed.*, 2005, **44**, 4670–4679.
6 I. Abánades Lázaro, X. Chen, M. Ding, A. Eskandari, D. Fairen-Jimenez, M. Giménez-Marqués, R. Gref, W. Lin, T. Luo and R. S. Forgan, *Nat. Rev. Methods Primers*, 2024, **4**, 42.
7 M. Gao, B. Song, D. Sensharma and M. J. Zaworotko, *SmartMat*, 2021, **2**, 38–55.
8 K. Lu, T. Aung, N. Guo, R. Weichselbaum and W. Lin, *Adv. Mater.*, 2018, **30**, 1707634.
9 T. Drake, P. Ji and W. Lin, *Acc. Chem. Res.*, 2018, **51**, 2129–2138.
10 B. Kesanli and W. Lin, *Coord. Chem. Rev.*, 2003, **246**, 305–326.
11 J.-L. Wang, C. Wang and W. Lin, *ACS Catal.*, 2012, **2**, 2630–2640.
12 K. Lu, C. He, N. Guo, C. Chan, K. Ni, G. Lan, H. Tang, C. Pelizzari, Y.-X. Fu, M. T. Spiotto, R. R. Weichselbaum and W. Lin, *Nat. Biomed. Eng.*, 2018, **2**, 600–610.
13 H.-Q. Yin, Z.-M. Zhang and T.-B. Lu, *Acc. Chem. Res.*, 2023, **56**, 2676–2687.
14 Y.-B. Huang, J. Liang, X.-S. Wang and R. Cao, *Chem. Soc. Rev.*, 2017, **46**, 126–157.
15 T. Wu, X.-J. Gao, F. Ge and H.-G. Zheng, *CrystEngComm*, 2022, **24**, 7881–7901.
16 W. Gong, Z. Chen, J. Dong, Y. Liu and Y. Cui, *Chem. Rev.*, 2022, **122**, 9078–9144.
17 S. Thoonen and C. Hua, *Chem. – Asian J.*, 2021, **16**, 890–901.
18 X. Zhang, J. Yin and J. Yoon, *Chem. Rev.*, 2014, **114**, 4918–4959.
19 W. Lin, *Top. Catal.*, 2010, **53**, 869–875.
20 C. Wang, T. Zhang and W. Lin, *Chem. Rev.*, 2012, **112**, 1084–1104.
21 H.-L. Qian, S.-T. Xu and X.-P. Yan, *Anal. Chem.*, 2023, **95**, 304–318.
22 C. Deng, B.-Q. Song, M. Lusi, A. A. Bezrukov, M. M. Haskins, M.-Y. Gao, Y.-L. Peng, J.-G. Ma, P. Cheng, S. Mukherjee and M. J. Zaworotko, *Cryst. Growth Des.*, 2023, **23**, 5211–5220.
23 S. J. Lee and W. Lin, *J. Am. Chem. Soc.*, 2002, **124**, 4554–4555.
24 M. M. Wanderley, C. Wang, C.-D. Wu and W. Lin, *J. Am. Chem. Soc.*, 2012, **134**, 9050–9053.
25 Z. Han, K. Wang, H. Min, J. Xu, W. Shi and P. Cheng, *Angew. Chem., Int. Ed.*, 2022, **61**, e202204066.
26 S. Li, Y. Zhou and B. Yan, *Inorg. Chem.*, 2022, **61**, 9615–9622.
27 Y.-W. Zhao, L.-E. Guo, F.-Q. Zhang, J. Yao and X.-M. Zhang, *ACS Appl. Mater. Interfaces*, 2021, **13**, 20821–20829.
28 H. Wei, H. Shen, B. Wang, X. You, X. Zhang, L. Fan and L. Tang, *CNIPA*, CN115745764A, 2023.
29 P. Machin, A. Sharpe, C. J. Lock, M. S. Chambers, A. Hodges and V. Allen, *WIPO*, WO2016098005A1, 2016.
30 A. Marfat, R. J. Chambers, J. W. Watson, J. B. Cheng, A. J. Duplantier and E. F. Kleinman, *WIPO*, WO9845268, 1997.
31 Z. Fei, M. Zhang, S. Xie and L. Yuan, *Electrophoresis*, 2014, **35**, 3541–3548.
32 R. Hailili, L. Wang, J. Qv, R. Yao, X.-M. Zhang and H. Liu, *Inorg. Chem.*, 2015, **54**, 3713–3715.
33 L. Ma, C. D. Wu, M. M. Wanderley and W. Lin, *Angew. Chem., Int. Ed.*, 2010, **49**, 8244–8248.
34 J. R. Lakowica, Quenching of Fluorescence, in *Principles of Fluorescence Spectroscopy*, Springer, New York, NY, 3rd edn, 2006, pp. 277–330.
35 J. Keizer, *J. Am. Chem. Soc.*, 1983, **105**, 1494–1498.
36 T. Kohlmann and M. Goez, *Phys. Chem. Chem. Phys.*, 2019, **21**, 10075–10085.